Journal of Computational Acoustics, Vol. 3, No. 4 (1995) 261-280

SOME ASPECTS OF THE PHYSICS AND NUMERICAL MODELING OF BIOT COMPRESSIONAL WAVES

JOSÉ M. CARCIONE and GERARDO QUIROGA-GOODE
Osservatorio Geofisico Sperimentale, P.O. Box 2011 Opicina, 34016 Trieste, Italy
carcione@gems755.ogs.trieste.it & quiroga@gems755.ogs.trieste.it

Communicated by V. L. Pereyra

Received 15 September 1994
Revised 10 January 1995

We investigate the problem of wave propagation in a porous medium, in the framework of Biot's theory, computing the numerical solution of the differential equations by a grid method. The problems posed by the stiffness of the equations are circumvented by using a partition (or splitting) time integrator which allows for an efficient explicit solution as in the case of nonstiff differential equations. The resulting algorithm possesses fourth-order accuracy in time and "infinite" (spectral) accuracy in space. Alternatively, a second-order algorithm, based on a Crank-Nicolson method, provides similar stability properties, although lower accuracy. The simulations correctly reproduce the wave forms of the fast and slow compressional waves and their relative amplitudes. Moreover, we observe the static slow mode, particularly strong when the source is a bulk perturbation or a fluid volume injection. The numerical results are confirmed by the analytical solution.

1. Introduction

The acoustics of porous media arise in a variety of geophysical contexts and engineering applications.[1,5] The most popular theory was developed by Biot[2-4] who obtained the dynamical equations for wave propagation in a saturated medium. The theory assumes that the anelastic effects arise from viscous interaction between the fluid and the solid and predicts two compressional waves and one shear wave. The fast compressional wave has solid and fluid displacement in phase, and the slow compressional wave has out of phase displacements. At low frequencies, the medium does not support the slow wave, which becomes diffusive, since the fluid viscosity effects dominate over the inertial effects. At high frequencies, the inertial effects are predominant and the slow mode is activated.

The dynamical equation has the form $\dot{\mathbf{V}} = \mathbf{M}\mathbf{V}$, where $\mathbf{V}$ is the wave field vector and $\mathbf{M}$ is the propagation matrix (the dot denotes time differentiation). All the eigenvalues of $\mathbf{M}$ have negative real part. While the eigenvalues of the fast wave have a small real part, the eigenvalues of the slow wave (in the diffusive regime) have a large real part. The presence of this diffusive mode makes Biot's differential equations *stiff*.[14] This condition practically precludes the use of standard explicit time integration techniques since they require a very

small time step to satisfy the stability condition. In this work, we suggest two explicit integration algorithms that possess the efficiency of implicit methods in terms of numerical stability. The first algorithm is based on a staggered second-order Crank–Nicolson method and the second is a splitting technique that yields the analytical solution of the stiff part, and the solution of the nonstiff part by a high-order scheme.

Since the presence of the shear wave is not relevant to this work, we consider the poroacoustic version of Biot's equations, i.e., with the rigidity of the matrix equal to zero. They describe wave motion in a colloid that can be considered as an emulsion or a gel.[13] It is an emulsion since shear waves do not propagate. On the other hand, since the "frame" modulus is different from zero, the "solid" component provides a sufficient structural framework for rigidity, and therefore can be considered as a gel. The results reveal the presence of the static slow mode, particularly strong in the fluid pressure, when the source is a fluid volume injection.

Previous works dealing with the simulation of Biot waves with direct grid methods are relatively scarce. Garg *et al.*[10] computed 1-D Green's functions (artificially damped) with a finite difference method. Hassanzadeh[11] and Zhu and McMechan[18] used standard (explicit) finite differences methods to solve the poroacoustic and poroelastic Biot's equations, respectively. On the other hand, Dai *et al.*[9] use a McCormack scheme, second-order in time, fourth-order in space, based on a dimensional splitting technique. All these works do not report the presence of the slow static mode, and obtain stable solutions despite the fact that some of them use standard explicit schemes with coarse time steps.

This paper is organized as follows. The following section introduces the velocity-pressure formulation of Biot's poroacoustic equations. Then, Sec. 3 analyzes the eigenvalues of the propagation matrix in order to quantify the stiffness of the problem. Section 4 presents the two explicit algorithms for time integrating the equations. Finally, Sec. 5 presents the simulations, which are verified with the analytical transient solution. Special emphasis is given to the static mode which is particularly strong in the fluid pressure wave field.

2. Wave Equation

The dynamical equations describing wave propagation in a heterogeneous porous media are given by Biot[3,4] who, generalizing a previous work,[2] considers variations of the porosity. Therefore, the numerical modeling based on a heterogeneous approach should not use Biot's equations given in Ref. 2, since they are formulated in the context of uniform porosity. By taking the solid rigidity equal to zero, we only model dilatational deformations, i.e., the compressional waves. The 2-D velocity-pressure formulation of Biot's (low-frequency range) poro*acoustic* equations, in the (x, y)-plane, is

$$\dot{v}_x = \beta_{11}\partial_x p + \beta_{12}\partial_x p_f + \frac{\eta}{\kappa}\beta_{12} q_x\,, \tag{2.1}$$

$$\dot{v}_y = \beta_{11}\partial_y p + \beta_{12}\partial_y p_f + \frac{\eta}{\kappa}\beta_{12} q_y\,, \tag{2.2}$$

$$\dot{q}_x = -\beta_{21}\partial_x p - \beta_{22}\partial_x p_f - \frac{\eta}{\kappa}\beta_{22} q_x\,, \tag{2.3}$$

$$\dot{q}_y = -\beta_{21}\partial_y p - \beta_{22}\partial_y p_f - \frac{\eta}{\kappa}\beta_{22} q_y \,, \tag{2.4}$$

$$\dot{p} = -H(\partial_x v_x + \partial_y v_y) - C(\partial_x q_x + \partial_y q_y) + \dot{s} \,, \tag{2.5}$$

$$\dot{p}_f = -C(\partial_x v_x + \partial_y v_y) - M(\partial_x q_x + \partial_y q_y) + \dot{s}_f \,, \tag{2.6}$$

where the v's and the q's are the solid and fluid (relative to the solid) particle velocities, and p and p_f are the bulk and fluid pressures, respectively. Here,

$$H = \left[\frac{1}{K_m} - \frac{1}{K_s} - \phi\left(\frac{1}{K_s} - \frac{1}{K_f}\right)\right]\frac{1}{K} \,, \tag{2.7}$$

$$C = \left(\frac{1}{K_m} - \frac{1}{K_s}\right)\frac{1}{K} \,, \tag{2.8}$$

$$M = \frac{1}{K_m}\frac{1}{K} \,, \tag{2.9}$$

with

$$K = \phi\frac{1}{K_m}\left(\frac{1}{K_f} - \frac{1}{K_s}\right) + \frac{1}{K_s}\left(\frac{1}{K_m} - \frac{1}{K_s}\right) \,, \tag{2.10}$$

where K_s, K_m and K_f are the bulk moduli of the solid, matrix and fluid, respectively, and ϕ is the effective porosity. Moreover, η is the dynamic fluid viscosity and κ is the global permeability. Finally,

$$\begin{bmatrix} \beta_{11} & \beta_{12} \\ \beta_{21} & \beta_{22} \end{bmatrix} = \frac{1}{\rho_f^2 - \rho m}\begin{bmatrix} m & -\rho_f \\ \rho_f & -\rho \end{bmatrix} \,, \tag{2.11}$$

where $\rho = (1-\phi)\rho_s + \phi\rho_f$ is the composite density, with ρ_s and ρ_f being the solid and fluid densities respectively, and $m = \alpha\rho_f/\phi$ where α is the tortuosity, a dimensionless parameter that depends on the pore geometry.

The application of the source considers three cases (Carcione and Quiroga-Goode, 1994):

(i) bulk source: this case assumes that the energy is partitioned between the two phases. In this case (Hassanzadeh, 1991), the relation between the solid and fluid source strengths is equal to $(1/\phi)-1$. In the above velocity-pressure formulation this means that $s = s_f$.
(ii) solid source: in this case, $s_f = 0$.
(iii) fluid volume injection: in this case, $s = \phi s_f$.

3. Eigenvalues of the Propagation Matrix

The system of equations (2.1)–(2.6) can be written in matrix form as

$$\frac{d\mathbf{V}}{dt} = \mathbf{M}\mathbf{V} + \mathbf{S} \,, \tag{3.12}$$

where

$$\mathbf{V} = [v_x,\, v_y,\, q_x,\, q_y,\, p,\, p_f]^{\mathrm{T}} \tag{3.13}$$

is the unknown vector, $\mathbf{M}$ is the propagation matrix, which contains the spatial derivative and material parameters of the medium, and

$$\mathbf{S} = [0,\ 0,\ 0,\ 0,\ \dot{s},\ \dot{s}_f]^{\mathrm{T}} \tag{3.14}$$

is the source vector. Let us consider the 1-D version of Eq. (3.12) with $\mathbf{S} = 0$. The plane wave

$$\mathbf{V} = \mathbf{V}_0 \exp[i(\omega_C t - kx)]\,, \tag{3.15}$$

where ω_C is the complex frequency and k is the wave number, is a solution of Eq. (3.12) and gives an eigenvalue equation for the eigenvalues $\lambda = i\omega_C$.[7] When using the Fourier pseudospectral method (e.g., Ref. 6) for computing the spatial derivatives, the wave numbers supported by the numerical mesh span from $k = 0$ to the Nyquist wave number $k = \pi/D_X$, where D_X is the grid spacing. Figure 1 represents the eigenvalues of matrix $\mathbf{M}$ in the complex λ-plane, where (a) $k = \pi/D_X$ and $\eta = 0$, (b) $k = 0$ and $\eta \neq 0$, and (c) $k = \pi/D_X$ and $\eta \neq 0$.

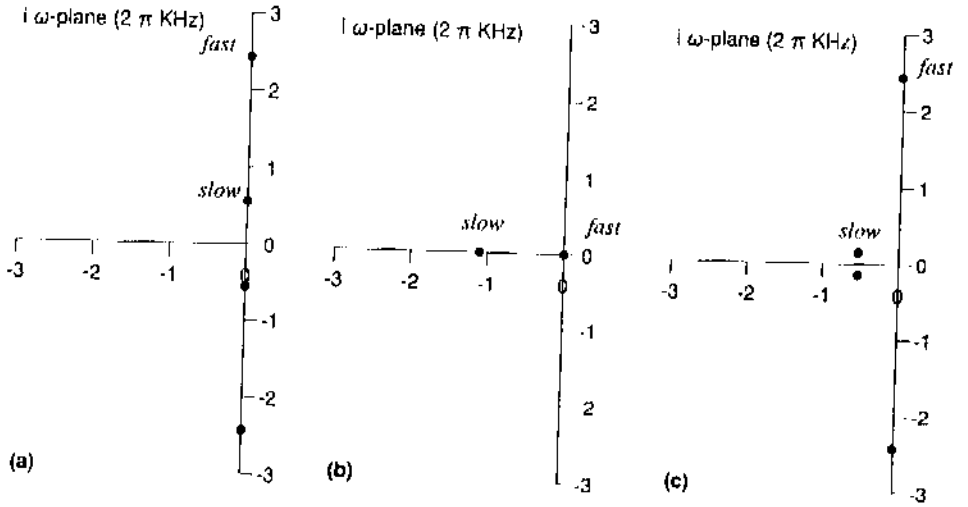

Fig. 1. Eigenvalues of the propagation matrix $\mathbf{M}$ in the $i\omega_C$-plane, where (a) $k = \pi/D_X$ and $\eta = 0$, (b) $k = 0$ and $\eta \neq 0$, and (c) $k = \pi/D_X$ and $\eta \neq 0$. The grid spacing is $D_X = 5$ cm and the material parameters are given in Table 1.

The eigenvalues come in complex conjugate pairs. When the fluid viscosity is zero, they lie in the imaginary axis, and describe propagating modes without dissipation. For a viscous fluid, the eigenvalues have a negative real part meaning that the waves are attenuated, in particular the slow wave. Precisely, the largest negative eigenvalue corresponds to the slow wave for $k = 0$:

$$\lambda_s = -(\eta/\kappa)\beta_{22}\,. \tag{3.16}$$

With the values in Table 1, $\lambda_s = -110301\ \mathrm{s}^{-1}$. In order to have numerical stability, the domain of convergence of the time integration scheme should include this eigenvalue. For instance, an explicit fourth-order Runge–Kutta method (Ref. 14, p. 71) requires

Table 1. Material properties for a brine saturated sandstone.

Solid	bulk modulus, K_s	40	GPa
	density, ρ_s	2500	kg/m^3
Matrix	porosity, ϕ	0.2	
	permeability, κ	600	mD
Fluid	bulk modulus, K_f	2.5	GPa
	density, ρ_f	1040	kg/m^3
	viscosity, η	1	cp

1 cp $= 10^{-3}$ Pa s; 1 mD $= 10^{-15}$ m^2

$dt\lambda_s > -2.78$, implying a very small time step dt. Then, the method is restricted by numerical stability rather than by accuracy. The presence of this large eigenvalue, together with small eigenvalues, indicates that the problem is *stiff* (Ref. 14, p. 72). In other words, the eigenvalues have negative real parts and differ greatly in magnitude. In stiff problems, the solution to be computed is slowly varying but perturbations exist that are rapidly damped. In this case, the perturbation is the slow wave, which, in the presence of fluid viscosity, presents a diffusive character.

4. Numerical Algorithms

As mentioned in the previous section, the spatial derivatives in Eqs. (2.1)–(2.6) are calculated with the Fourier method by using the FFT.[15] This approximation is infinitely accurate for band-limited periodic functions with cutoff spatial wave numbers which are smaller than the cutoff wave numbers of the mesh.

The stability problem posed by the eigenvalue λ_s can be solved if an A-stable method is used (Ref. 14, p. 73), implying stability in the open left-half-plane. To illustrate this problem, we first present a simple second-order method that possesess the stability properties of implicit algorithms but the solution can be obtained explicitly. Then, the high-order time splitting method is presented.

4.1. *Crank–Nicolson* $(2,\infty)$ *scheme*

The so-called A-stable methods include implicit integration schemes and therefore the solution of linear systems with its corresponding drawbacks. However, for Biot poroacoustic equations it is possible to obtain the solution *explicitly* even though the method is classified as implicit. The following time discretization of Eqs. (2.1)–(2.6):

$$D^{1/2}v_x = \beta_{11}\partial_x p^n + \beta_{12}\partial_x {p_f}^n + \frac{\eta}{\kappa}\beta_{12}A^{1/2}q_x\,, \tag{4.17}$$

$$D^{1/2}v_y = \beta_{11}\partial_y p^n + \beta_{12}\partial_y {p_f}^n + \frac{\eta}{\kappa}\beta_{12}A^{1/2}q_y\,, \tag{4.18}$$

$$D^{1/2}q_x = -\beta_{21}\partial_x p^n - \beta_{22}\partial_x {p_f}^n - \frac{\eta}{\kappa}\beta_{22}A^{1/2}q_x\,, \tag{4.19}$$

$$D^{1/2}q_y = -\beta_{21}\partial_y p^n - \beta_{22}\partial_y {p_f}^n - \frac{\eta}{\kappa}\beta_{22}A^{1/2}q_y\,, \tag{4.20}$$

$$D^1 p = -H(\partial_x A^{1/2}v_x + \partial_y A^{1/2}v_y) - C(\partial_x A^{1/2}q_x + \partial_y A^{1/2}q_y) + D^1 s\,, \tag{4.21}$$

$$D^1 p_f = -C(\partial_x A^{1/2}v_x + \partial_y A^{1/2}v_y) - M(\partial_x A^{1/2}q_x + \partial_y A^{1/2}q_y) + D^1 s_f\,, \tag{4.22}$$

where

$$D^j\phi = \frac{\phi^{n+j} - \phi^{n-j}}{2jdt}, \quad \text{and} \quad A^j\phi = \frac{\phi^{n+j} + \phi^{n-j}}{2}, \tag{4.23}$$

are the central differences and mean value operators, is based on a Crank–Nicolson (staggered) implicit scheme (Ref. 14, p. 269) for the particle velocities. In this three-level scheme, particle velocities variables at time $(n+1/2)dt$ and pressures at time $(n+1)dt$ are computed explicitly from particle velocities at time $(n-1/2)dt$ and pressures at time ndt and $(n-1)dt$. The explicit formulation requires first to compute ${q_x}^{n+1/2}$ and ${q_y}^{n+1/2}$ from (4.19) and (4.20), then compute ${v_x}^{n+1/2}$ and ${v_y}^{n+1/2}$ and finally, the pressures p^{n+1} and ${p_f}^{n+1}$. A similar sequence of computations is implemented by Virieux[17] to solve the *SH* wave equation.

The following is the Von Neumann stability analysis (Ref. 14, p. 418) based on the eigenvalues of the amplification matrix $\mathbf{G}$ defined below. Let us consider the 1-D case in the absence of sources. Since we use the Fourier pseudospectral method for computing the spatial derivatives, the difference operator is $\partial_x = ik$. Making this substitution in (4.17)–(4.22), we obtain the following matrix equation:

$$\mathbf{V}^+ = \mathbf{G}\mathbf{V}^-, \tag{4.24}$$

where

$$\mathbf{V}^+ = [v^{n+1/2},\, q^{n+1/2},\, p^{n+1},\, {p_f}^{n+1}] \tag{4.25}$$

and

$$\mathbf{V}^- = [v^{n-1/2},\, q^{n-1/2},\, p^{n-1},\, {p_f}^{n-1}]. \tag{4.26}$$

The von Neumann condition for stability is

$$\max|g_j| \le 1, \quad j = 1, \ldots, 4, \tag{4.27}$$

where g_j are the eigenvalues of the amplification matrix $\mathbf{G}$. For instance, $k = 0$ has

$$\mathbf{G} = \begin{bmatrix} 1 & \dfrac{dt(\eta/\kappa)\beta_{12}}{1+a} & 0 & 0 \\ 0 & \dfrac{1-a}{1+a} & 0 & 0 \\ 0 & 0 & 1 & 0 \\ 0 & 0 & 0 & 1 \end{bmatrix}, \tag{4.28}$$

where, by (3.16),

$$a = -\frac{1}{2}dt\lambda_s = \frac{1}{2}dt(\eta/\kappa)\beta_{22}\,.$$

Then, the eigenvalues are: 1, with multiplicity three, and

$$\frac{1-adt}{1+adt}, \quad a>0\,. \tag{4.29}$$

This leads to an unconditionally stable scheme (e.g., Ref. 16, p. 259). The use of the above implicit technique, although second-order, allows time steps of more than one order of magnitude larger than the explicit fourth-order Runge–Kutta and Taylor methods.

4.2. *Partition* $(4, \infty)$ *scheme*

A better time integration technique can be achieved by using a *partition* method (Ref. 12, p. 171). The stiff system (2.1–2.6) can be partitioned into two set of differential equations, one stiff and the other nonstiff, such that they can be treated by two different methods, one implicit and the other explicit, respectively. In this case, the stiff equations

$$\dot{v}_x = \frac{\eta}{\kappa}\beta_{12}q_x\,, \tag{4.30}$$

$$\dot{v}_y = \frac{\eta}{\kappa}\beta_{12}q_y\,, \tag{4.31}$$

$$\dot{q}_x = -\frac{\eta}{\kappa}\beta_{22}q_x\,, \tag{4.32}$$

$$\dot{q}_y = -\frac{\eta}{\kappa}\beta_{22}q_y\,, \tag{4.33}$$

can be solved analytically, giving

$$v_x^* = v_x^n - \frac{\beta_{12}}{\beta_{22}}[\exp(\lambda_s dt)-1]q_x^n\,, \quad v_y^* = v_y^n - \frac{\beta_{12}}{\beta_{22}}[\exp(\lambda_s dt)-1]q_y^n\,, \tag{4.34}$$

$$q_x^* = \exp(\lambda_s dt)q_x^n\,, \quad q_y^* = \exp(\lambda_s dt)q_y^n\,. \tag{4.35}$$

with λ_s given by Eq. (3.16). Note that, when $\eta = 0$, is $v^* = v^n$ and $q^* = q^n$, giving the purely elastic problem. As noted by Garg *et al.*,[10] strong viscous coupling leads to a single phase medium. This can be verified from Eqs. (4.32) and (4.33) by taking the limit $\eta \to \infty$. In this case, the relative fluid-solid motion vanishes, since $q_x \to 0$ and $q_y \to 0$.

The intermediate vector

$$\mathbf{V}^* = [v_x^*,\, v_y^*,\, q_x^*,\, q_y^*,\, p^n,\, p_f^n]^\top \tag{4.36}$$

is the input for an explicit high-order scheme that solves Eq. (3.12) with $\eta = 0$ to give $\mathbf{V}^{n+1}$. We use the fourth-order Runge–Kutta algorithm (Ref. 14, p. 68):

$$\mathbf{V}^{n+1} = \mathbf{V}^* + \frac{dt}{6}(\Delta_1 + 2\Delta_2 + 2\Delta_3 + \Delta_4)\,, \tag{4.37}$$

where

$$\Delta_1 = \mathbf{M}\mathbf{V}^* + \mathbf{S}^n\,, \tag{4.38}$$

$$\Delta_2 = \mathbf{M}\left(\mathbf{V}^* + \frac{dt}{2}\Delta_1\right) + \mathbf{S}^{n+1/2}\,, \tag{4.39}$$

$$\Delta_3 = \mathbf{M}\left(\mathbf{V}^* + \frac{dt}{2}\Delta_2\right) + \mathbf{S}^{n+1/2}\,, \tag{4.40}$$

$$\Delta_4 = \mathbf{M}(\mathbf{V}^* + dt\Delta_3) + \mathbf{S}^{n+1}\,. \tag{4.41}$$

This method is used in the next section to compute the simulations. These are verified by the analytical solution given in Appendix A, and are in agreement with the second-order scheme based on the Crank–Nicolson method. Appendix B presents the discrete dispersion equation of the partition scheme.

The advantage of the partition method is that the time step is determined by the algorithm that solves the nonstiff equations. As far as we are aware, time-splitting schemes have yet not been applied to elastodynamic problems. They are, however, standard practice in fluid dynamics (Ref. 6, p. 222).

5. Simulations

The material properties of the porous medium are given in Table 1, where the porosity corresponds to a typical reservoir sandstone. We consider that $K_m \approx K_s(1-\phi)$ and $\alpha = (1 + 1/\phi)/2$, which corresponds to spherical grains.[5] Figures 2(a) and 2(b) represent the phase velocities and attenuation curves of the compressional modes versus frequency, corresponding to the medium defined in Table 1. Here, we should keep in mind that the low-frequency Biot theory is valid for frequencies less than $\eta\phi/(2\pi\alpha\kappa\rho_f)$, which for the medium defined in Table 1 is approximately 17 kHz. As can be seen, the slow wave has a diffusive character at low frequencies. We note that the higher the frequency, the higher the dissipation, at least in the range where the low-frequency theory applies. This phenomenon, and the diffusive behavior of the slow wave at the low frequencies, makes it difficult to detect this wave experimentally over the whole frequency range. The performance of the numerical algorithm is verified with the analytical transient solution given in Appendix A. The modeling allows the calculation of the dilatational field in the solid and in the fluid. If we define the solid dilatation by e, and the fluid dilatation (relative to the solid) by ζ,[3] we have

$$\dot{\mathbf{E}} = \begin{bmatrix} \dot{e} \\ \dot{\zeta} \end{bmatrix} = \mathrm{div}\begin{bmatrix} \mathbf{v} \\ -\mathbf{q} \end{bmatrix}. \tag{5.42}$$

Then, it can be shown that, at every grid point, the dilatational vector can be computed as

$$\mathbf{E} = \mathbf{B}^{-1}\mathbf{P}\,, \tag{5.43}$$

where $\mathbf{P}$ and $\mathbf{B}$ are given by Eqs. (A.2) and (A.3) of Appendix A, respectively. In this case, $\mathbf{B}$ can be space-dependent.

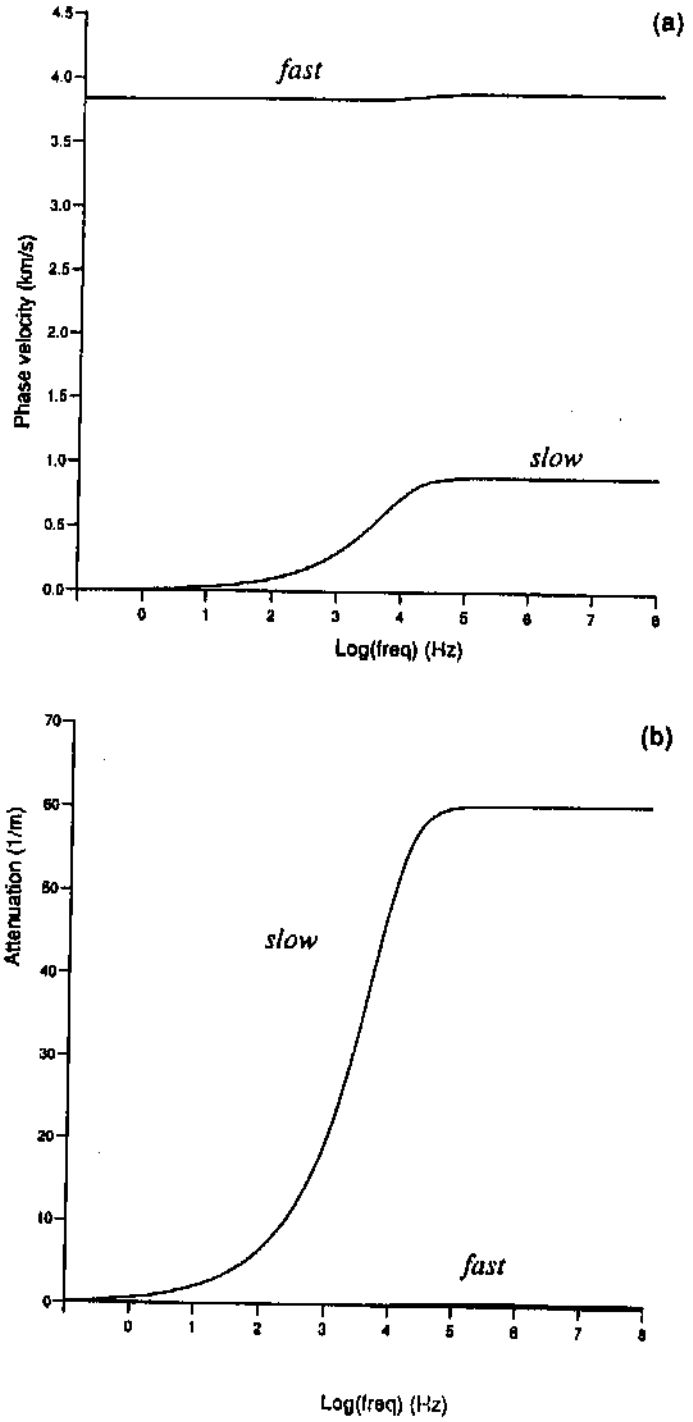

Fig. 2. Phase velocities (a) and attenuation (b) curves versus frequency

The numerical mesh has $N_X = N_Y = 225$ points, and the simulations are carried out in two different frequency ranges. In the *seismic* range we take a grid spacing of $D_X = D_Y = 10$ m, and a source central frequency of $f_c = 22$ Hz, while in the *sonic* range, $D_X = D_Y = 5$ cm and $f_c = 4.5$ kHz. Therefore, the size of the meshes are 2240 m and 11.2 m for the seismic and sonic ranges, respectively. The source terms s and s_f consist of

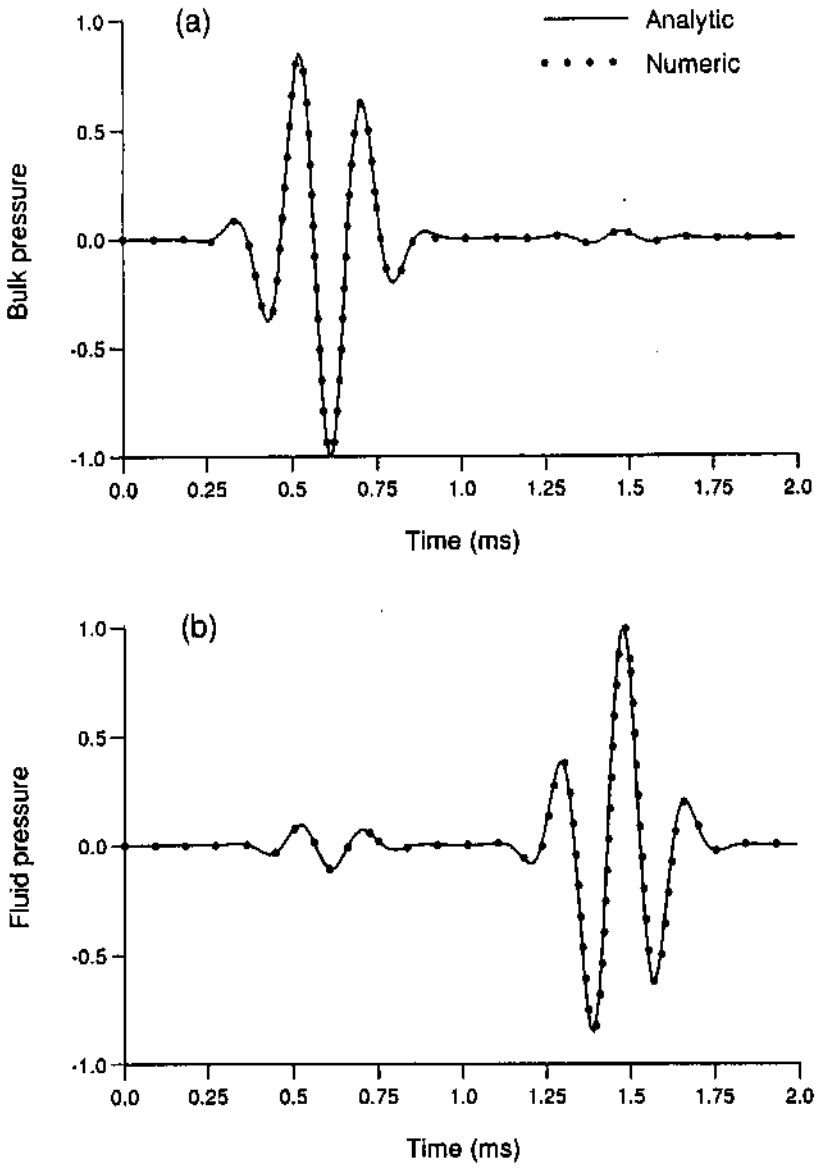

Fig. 3. Comparison between numerical and analytical time histories at a distance of 1 m from the source, where: (a) bulk pressure ($\eta = 0$), (b) fluid pressure ($\eta = 0$), (c) bulk pressure ($\eta \neq 0$) and (d) fluid pressure ($\eta \neq 0$) are considered. The source is in the solid phase and has a central frequency of 4.5 kHz.

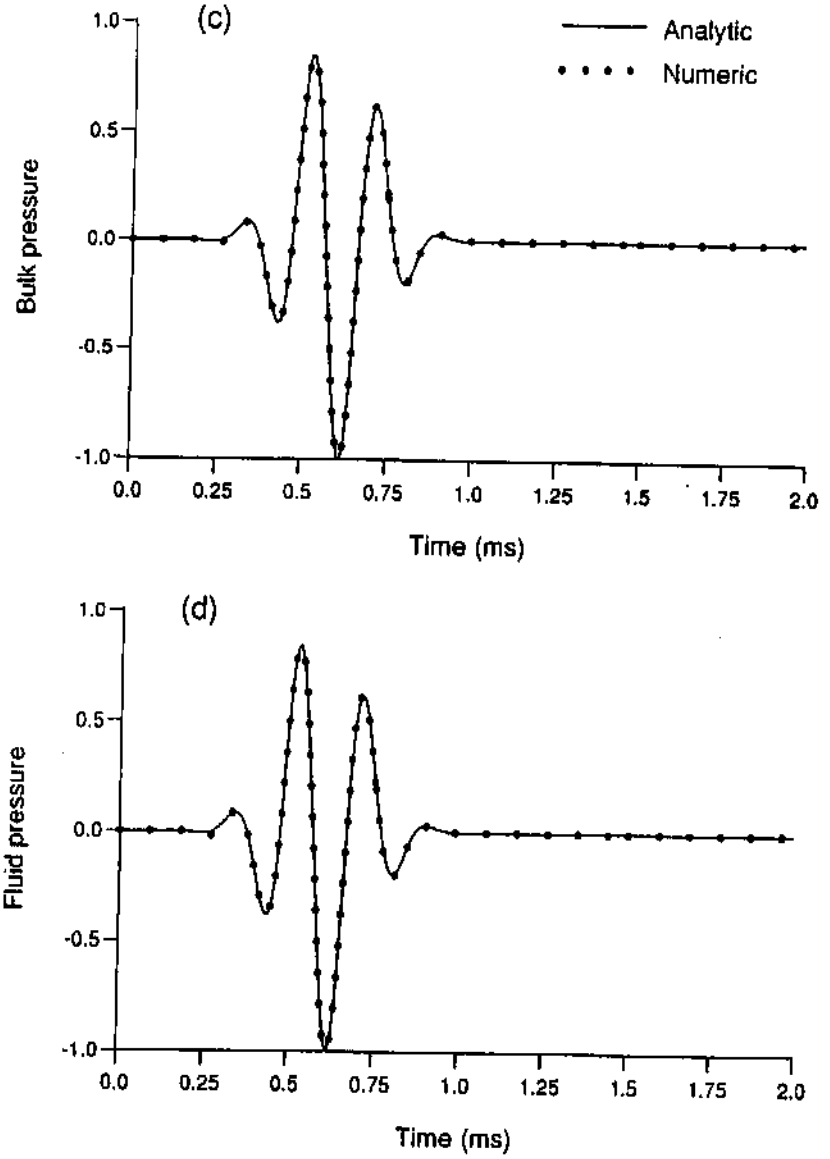

Fig. 3. (*Continued*)

a discrete spatial delta function multiplied by the time function

$$f(t) = \exp\left[-\frac{1}{2}f_c^2(t-t_o)^2\right]\cos[\pi f_c(t-t_o)]\,, \tag{5.44}$$

where $t_o = 3/f_c$.

Numerical and analytical (sonic) time histories are compared in Fig. 3, where (a) and (b) correspond to the bulk and fluid pressures for $\eta = 0$, respectively, and (c) and (d) are the bulk and fluid pressures for $\eta \neq 0$, respectively. The source is in the solid phase, and the receiver is located 1 m apart. The matching between solutions is virtually perfect.

In the following simulations, the source term is such that $\mathbf{S} \propto f(t)$, where $\mathbf{S}$ is defined in Eq. (3.14). Then, for comparison with the analytical solution, the Green's function (A.9) has to be divided by the factor $i\omega$. Figures 4 and 5 compare numerical and analytical (sonic) snapshots of the bulk and fluid pressures, corresponding to $\eta = 0$ and $\eta \neq 0$, respectively.

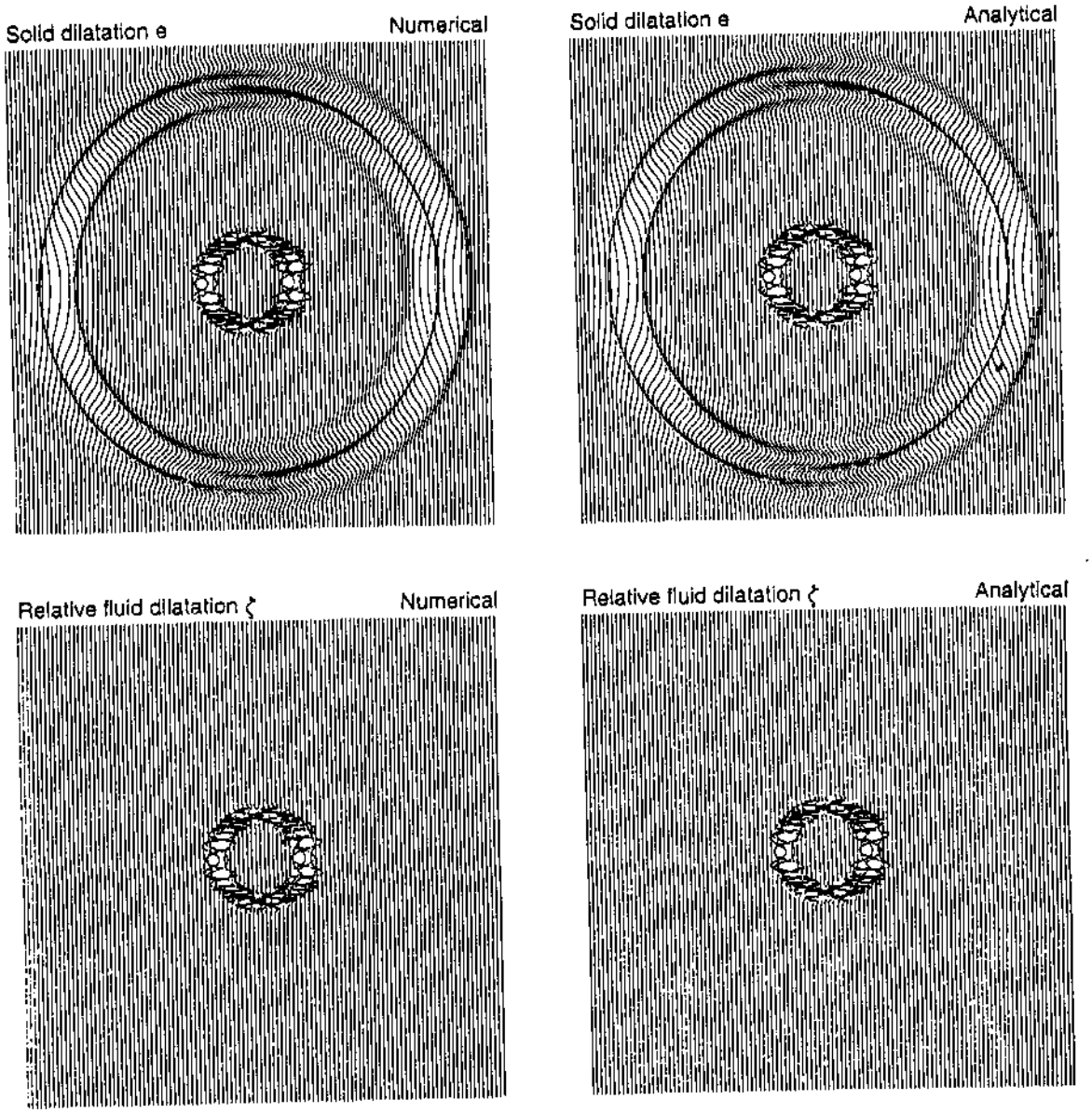

Fig. 4. (a) Comparison of numerical and analytical snapshots $\eta = 0$. The perturbation is a bulk source with a central frequency of 4.5 kHz. (b) Comparison of numerical and analytical snapshots $\eta \neq 0$. The perturbation is a bulk source with a central frequency of 4.5 kHz.

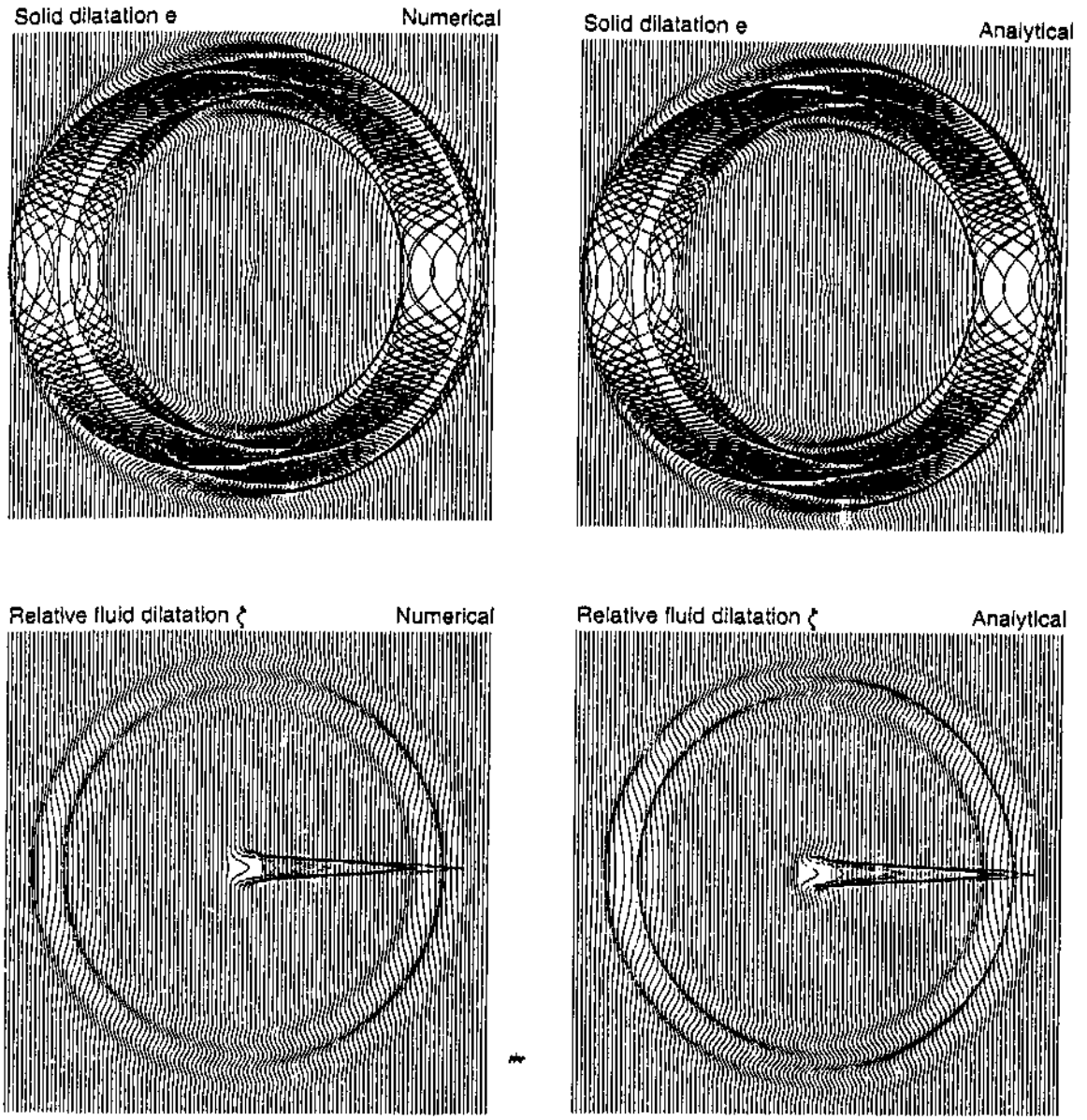

(b)

Fig. 4. (*Continued*)

The source is in the bulk material and the propagation time is 1.5 ms. As can be seen, the modeling results coincide with the analytical solutions. When the fluid is viscous, the slow wave becomes diffusive and appears as a static mode at the source location. In this case, the numerical and analytical solutions differ slightly. The fact that the Hankel

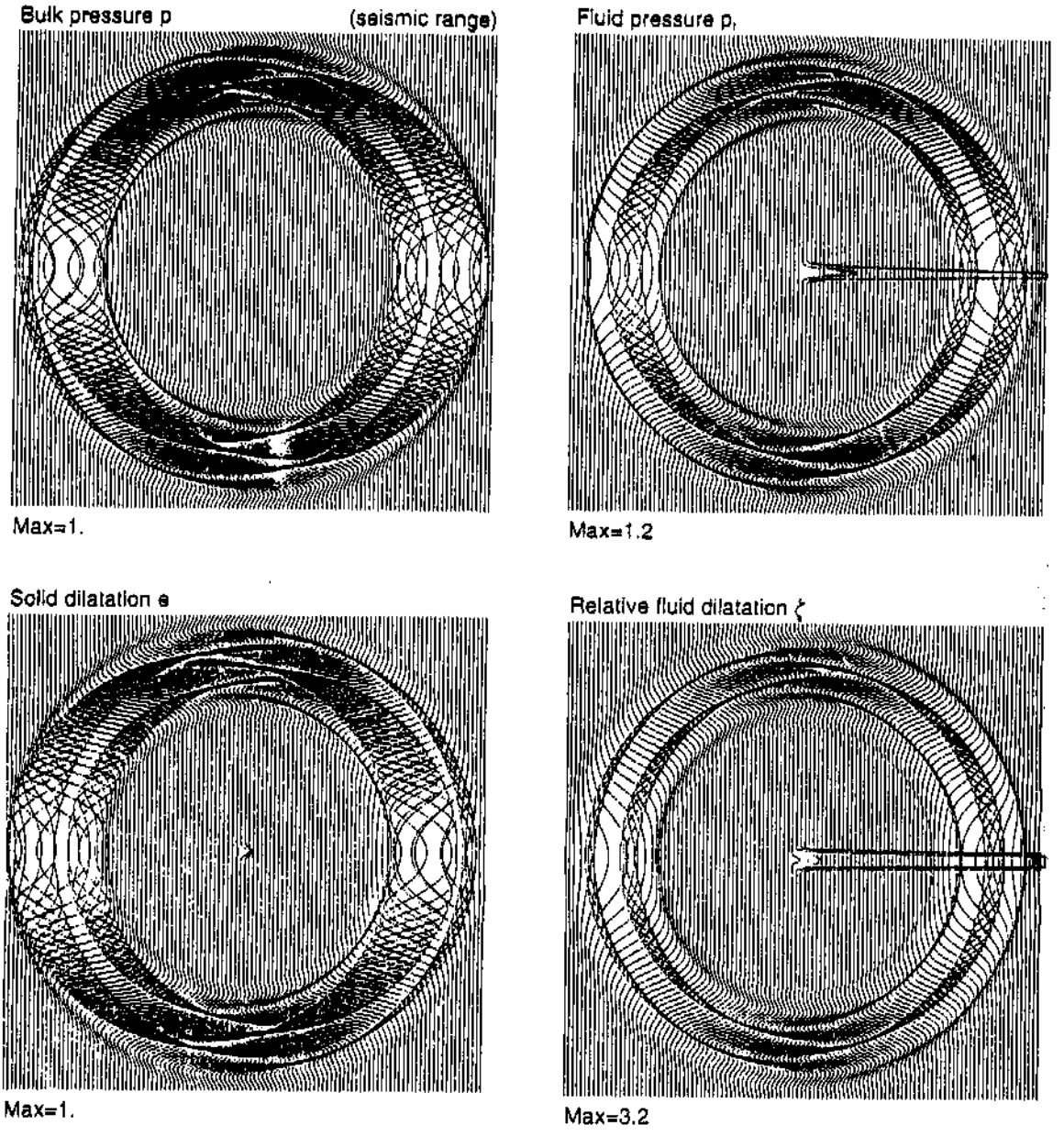

Fig. 5. Snapshots of the pressures and dilatations in the seismic range ($D_X = D_Y = 10$ m and $f_c = 22$ Hz), for a bulk source. The propagation time is 0.3 s and the medium is defined in Table 1. The amplitudes are scaled with respect to the maximum bulk pressure and maximum solid dilatation.

function is singular for $\omega = 0$ and at the source location ($r = 0$) may introduce errors in the calculation of the analytical solution. On the other hand, the choice $D_X = 5$ cm in the numerical modeling, together with the very low velocities of the slow mode (see Fig. 3), violates the sampling theorem. This could produce aliasing of the static mode (although numerical experiments with smaller grid spacing yield the same results as in Figs. 4

and 5). Figure 6 represents snapshots of the pressures and dilatations in the seismic range, at 0.3 s propagation time. The source is in the bulk material. The amplitudes are scaled with respect to the maximum bulk pressure and maximum solid dilatation. We observe two events, the fast wave and the static slow wave at the location of the source (the latter is clipped when exceeding the frame of the snapshot). Figure 2(a) indicates that the phase

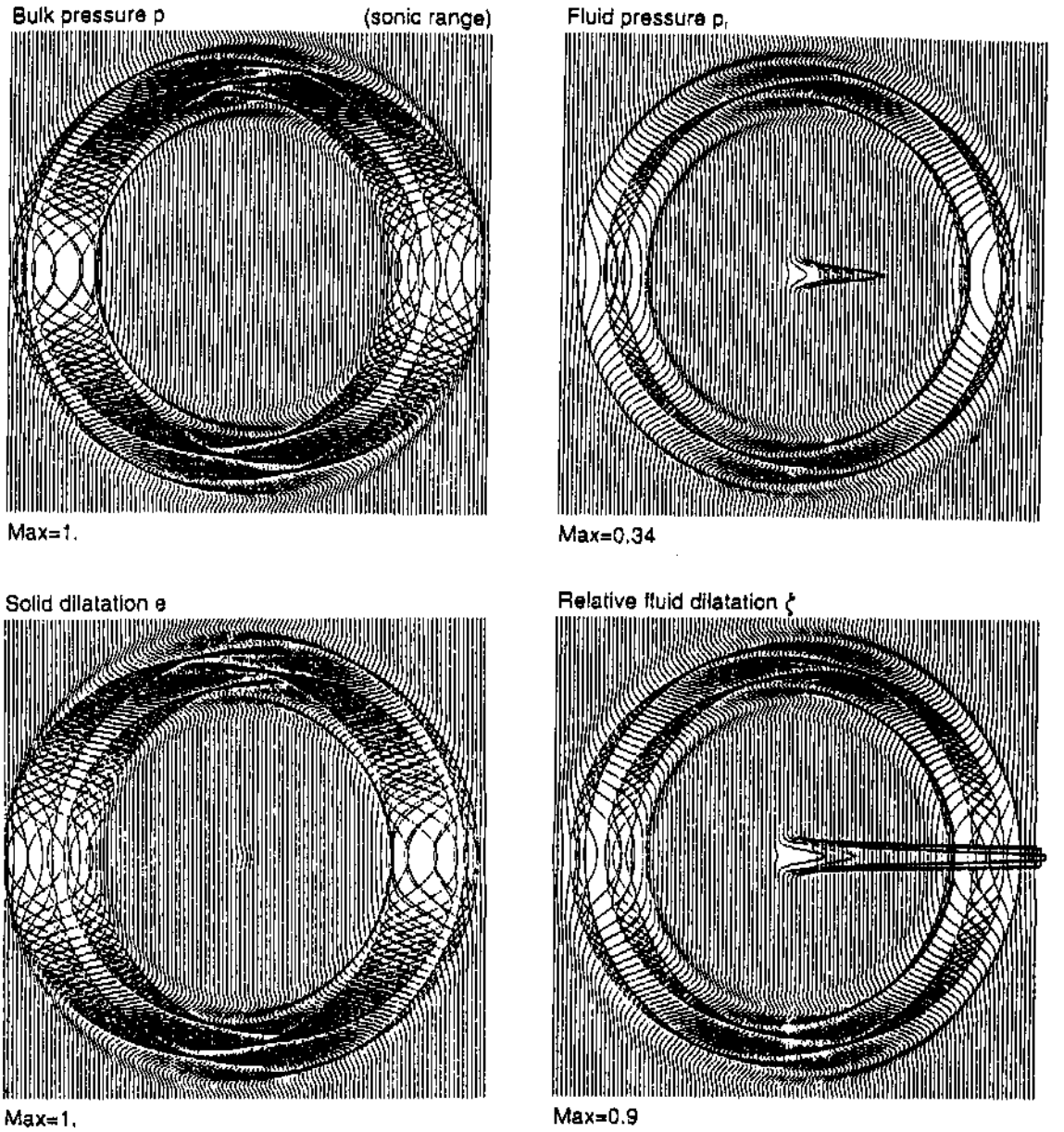

Fig. 6. Snapshots of the pressures and dilatations in the sonic range ($D_X = D_Y = 5$ cm and $f_c = 4.5$ kHz), for a bulk source. The propagation time is 1.5 ms and the medium is defined in Table 1. The amplitudes are scaled with respect to the maximum bulk pressure and maximum solid dilatation.

velocity of the static mode for 22 Hz is close to zero, implying a diffusive behavior. The static mode is stronger in the fluid pressure and relative fluid dilatation. It can be shown that a fluid source generates a stronger static mode than a bulk source. Moreover, dilatations are more sensitive to this mode than pressures. The amplitudes are scaled with respect to the maximum bulk pressure and maximum solid dilatation. The main differences are that, in the sonic range, this mode is relatively weaker and spatially broader.

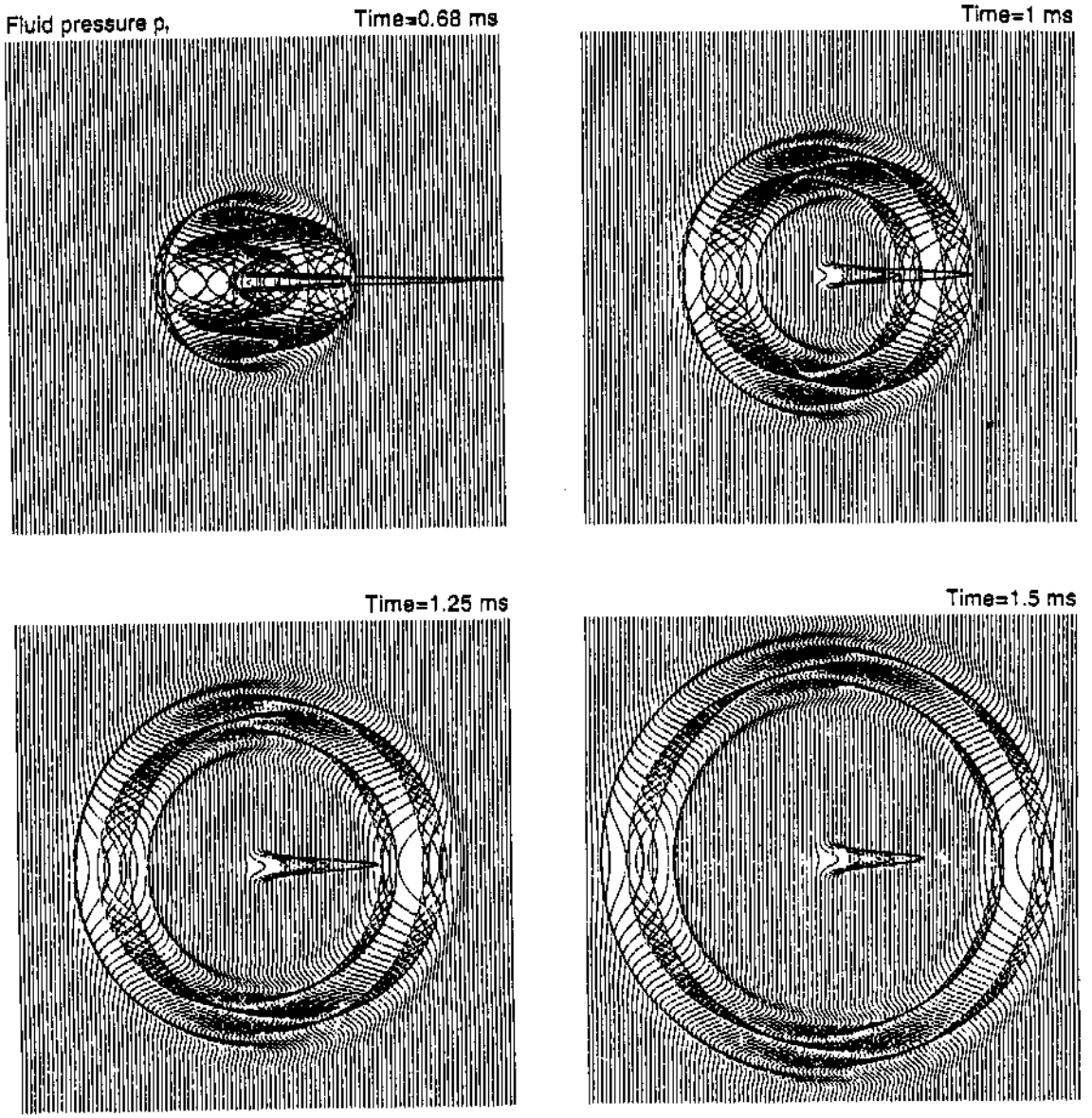

Fig: 7. Successive snapshots of the fluid pressure in the sonic range ($D_X = D_Y = 5$ cm and $f_c = 4.5$ kHz) showing the damping of the slow static mode. The perturbation is a bulk source.

We see in Fig. 2(a) that the phase velocity of the slow wave at the central frequency of the source (4.5 kHz) is about 300 m/s. This could suggest that the behavior of the slow mode is propagative. In fact, the pulse is broader than in the seismic case, however, as can be seen in Fig. 2(b), the high attenuation at that frequency precludes the propagation.

Figure 6 represents snapshots of the pressures and dilatation in the sonic range, at 1.5 ms propagation time. The source is in the bulk material.

The temporal dissipation of the slow mode can be seen in Fig. 7, where snapshots of the fluid pressure at different propagation times are represented. The source is a bulk perturbation with a duration of 0.68 ms. The amplitude of the static mode is determined by the factor $\exp(\lambda_s t)$ where λ_s is given by Eq. (3.16).

6. Conclusions

The differential equations describing wave propagation in a porous medium are stiff. Therefore, the super stability of the equations turns out to be disadvantageous for the error propagation of classical explicit time integration methods. The partition (or splitting) method, proposed in this work, solves the stiff part analytically, and the nonstiff part by using a high-order explicit scheme, allowing the use of a coarse time step. The modeling correctly reproduces the amplitude and propagation of the fast and slow compressional modes, including the static slow mode when the fluid viscosity is different from zero. The results are confirmed by the analytical solution and are in agreement with a second-order time integration scheme based on the implicit Crank–Nicolson method. The simulations indicate that the slow compressional wave and the static slow mode are stronger in the fluid and when a fluid volume injection is used as source.

Acknowledgments

This work was funded in part by the European Commission in the framework of the JOULE programme, sub-programme Advanced Fuel Technologies. Dr. Fabio Cavallini kindly read the manuscript and made helpful suggestions.

Appendix A. Poroacoustic Analytical Solution

Carcione and Quiroga-Goode[8] obtained the transient solution for wave propagation in 2-D and 3-D homogeneous viscoelastic porous media, valid at the low and high frequency ranges. Here, we outline the 2-D low-frequency elastic solution assuming an acoustic frame.

It can be shown that the frequency-domain version of Eqs. (2.1)–(2.6) is, in compact form:

$$\Delta(\mathbf{P}-\mathbf{F})+\omega^2\boldsymbol{\Gamma}\mathbf{B}^{-1}\mathbf{P}=0\,, \tag{A.1}$$

where .

$$\mathbf{P}=[p,\,p_f]^{\top}\,,\quad \mathbf{F}=[s,\,s_f]^{\top}\,, \tag{A.2}$$

and

$$\mathbf{B} = \begin{bmatrix} -H & C \\ -C & M \end{bmatrix}, \quad \mathbf{\Gamma} = \begin{bmatrix} -\rho & \rho_f \\ -\rho_f & m - \dfrac{i}{\omega}\dfrac{\eta}{\kappa} \end{bmatrix}. \tag{A.3}$$

Note that the matrix defined in Eq. (2.11) equals $\mathbf{\Gamma}^{-1}(\eta = 0)$ and that $\mathbf{F} \propto i\omega f(\omega)$, with $f(t)$ defined in Eq. (5.44). The frequency-domain solution is

$$\mathbf{P}(\mathbf{x}, \omega) = \Delta\mathbf{G}(\mathbf{x}, \omega)\hat{\mathbf{F}}(\omega), \tag{A.4}$$

where $\mathbf{G}$ is the Green's function given by[8]

$$\mathbf{G}(\omega) = \frac{1}{V_2^2 - V_1^2}\{(V_1V_2)^2[g(V_1) - g(V_2)]\mathbf{\Gamma}\mathbf{B}^{-1} + [V_2^2 g(V_2) - V_1^2 g(V_1)]\mathbf{I}\}, \tag{A.5}$$

with

$$V_{1(2)}^2 = \frac{2\det\mathbf{B}}{U \pm (U^2 - 4\det\mathbf{B}\det\mathbf{\Gamma})^{1/2}} \tag{A.6}$$

$$U = 2\rho_f C - \rho M - H\left(m - \frac{i}{\omega}\frac{\eta}{\kappa}\right),$$

defining the complex velocities V_1 and V_2 of the fast (+ sign) and slow (− sign) compressional waves. The corresponding 2-D Green's functions ($m = 1, 2$) are

$$g(V_m) = -iH_0^{(2)}\left(\frac{\omega}{V_m}r\right), \quad r = (x^2 + y^2)^{1/2}, \tag{A.7}$$

where $H_0^{(2)}$ is the Hankel function of the second kind. Moreover, $\hat{\mathbf{F}} = [\hat{s}, \hat{s}_f]^\top$, with $\hat{s}$ and $\hat{s}_f$ frequency dependent only (through the source spectrum). They are related as indicated at the end of Sec. 2. To compute the Laplacian of the Green's function we use the property

$$\Delta g(V_m) = -\left[4\delta(\mathbf{x}) + \left(\frac{\omega}{V_m}\right)^2 g(V_m)\right]. \tag{A.8}$$

This gives

$$\Delta\mathbf{G}(\omega) = \frac{\omega^2}{V_2^2 - V_1^2}\{[V_1^2 g(V_2) - V_2^2 g(V_1)]\mathbf{\Gamma}\mathbf{B}^{-1} + [g(V_1) - g(V_2)]\mathbf{I}\} - 4\delta(\mathbf{x})\mathbf{I}. \tag{A.9}$$

The time-domain solution is obtained by a numerical inverse time Fourier transform.

Appendix B. Dispersion Equation

In this Appendix, we calculate the dispersion equation of Biot's equations (2.1)–(2.6) after time discretization with the partition method. Since the stiff part is computed analytically, we only need to consider the dispersion equation obtained with the Runge–Kutta algorithm ($\eta = 0$). Let us assume the 1-D case and a plane wave of the form

$$\mathbf{U}^n = \mathbf{U}_0 \exp[i(\omega n dt - k_C x)], \tag{B.1}$$

where k_C is the complex wave number, and

$$\mathbf{U} = [v, -q, p, p_f]^\top . \tag{B.2}$$

It can be seen that Eq. (3.12) (with $\eta = 0$) for the plane wave (B.1) becomes

$$\frac{d\mathbf{U}}{dt} = ik_C \mathbf{M}'\mathbf{U} , \tag{B.3}$$

where

$$\mathbf{M}' = \begin{bmatrix} \mathbf{0} & \boldsymbol{\Gamma}^{-1} \\ \mathbf{B} & \mathbf{0} \end{bmatrix} . \tag{B.4}$$

with $\mathbf{0}$ denoting the 2×2 zero matrix, and $\mathbf{B}$ and $\boldsymbol{\Gamma}$ given in Appendix A.

On the other hand, it is easy to show that the Runge–Kutta method yields (Ref. 14, p. 71):

$$\mathbf{U}^{n+1} = \left[\mathbf{I} + ik_C\mathbf{M}'dt + \frac{1}{2}(ik_C\mathbf{M}'dt)^2 + \frac{1}{6}(ik_C\mathbf{M}'dt)^3 + \frac{1}{24}(ik_C\mathbf{M}'dt)^4\right]\mathbf{U}^n . \tag{B.5}$$

Substitution of Eq. (B.1) into Eq. (B.5) gives the dispersion equation:

$$\det\left[(1 - \exp i\omega dt)\mathbf{I} + ik_C\mathbf{M}'dt + \frac{1}{2}(ik_C\mathbf{M}'dt)^2 + \frac{1}{6}(ik_C\mathbf{M}'dt)^3 + \frac{1}{24}(ik_C\mathbf{M}'dt)^4\right] = 0 , \tag{B.6}$$

where the unknown is the complex wave number k_C which, in the discrete case, is complex and frequency-dependent. The complex velocity can be defined as

$$V = \frac{\omega}{k_C} , \tag{B.7}$$

and the phase velocity V_p as the frequency divided by the real part of the wave number. It gives

$$V_p = \left(\Re\left[\frac{1}{V}\right]\right)^{-1} . \tag{B.8}$$

The dispersion equation for the continuous case is obtained when $dt \to 0$. Then, $\exp i\omega dt \approx 1 + i\omega dt$, and neglecting second-order terms in dt, we obtain

$$\det(\mathbf{M}' - V\mathbf{I}) = 0 . \tag{B.9}$$

In this case V is real and frequency-independent, and is given by Eq. (A.6) with $\eta = 0$. This can be easily demonstrated from the fact that, if V is an eigenvalue of $\mathbf{M}'$, then V^2 is an eigenvalue of $\mathbf{B}\boldsymbol{\Gamma}^{-1}$.

References

1. J. F. Allard, *Propagation of Sound in Porous Media: Modeling Sound Absorbing Materials* (Elsevier Pub. Ltd., 1993).
2. M. A. Biot, *J. Acous. Soc. Am.* **28** (1956) 168–178.

3. M. A. Biot, *J. Appl. Phys.* **33** (1962) 1482–1498.
4. M. A. Biot, *J. Acous. Soc. Am.* **82** (1962) 1254–1264.
5. T. Bourbie, O. Coussy, and B. Zinszner, *Acoustics of Porous Media* (Institute Francais du Petrole Pub., 1987).
6. C. Canuto, M. Y. Hussaini, A. Quarteroni, and T. A. Zang, *Spectral Methods in Fluid Dynamics* (Springer-Verlag, 1988).
7. J. M. Carcione, *Eur. J. Mech, A/Solids* **12** (1993) 53–71.
8. J. M. Carcione and G. Quiroga-Goode, "Full frequency-range transient solution for compressional waves in a fluid-saturated viscoelastic porous medium," submitted to *Geophysical Prospecting*, 1994.
9. N. Dai, A. Vafidis, and E. R. Kanasewich, "Wave propagation in porous media: High-order finite difference solution to Biot's equations," submitted to *Geophysics*, 1992.
10. S. K. Garg, A. H. Nayfeh, and A. J. Good, *J. Appl. Phys.* **45** (1974) 1968–1974.
11. S. Hassanzadeh, *Geophys.* **56** (1991) 424–435.
12. E. Hairer and G. Wanner, *Solving Ordinary Differential Equations II* (Springer-Verlag, 1991).
13. R. J. Hunter, *Foundations of Colloidal Science* (Clarendon Press, 1987).
14. M. K. Jain, *Numerical Solutions of Differential Equations* (Wiley Eastern Ltd., 1984).
15. D. Kosloff, M. Reshef, and D. Loewenthal, *Bull. Seis. Soc. Am.* **74**, (1984) 875–891.
16. G. Sewel, *The Numerical Solutions of Ordinary and Partial Differential Equations* (Academic Press, Inc., 1988).
17. J. Virieux, *Geophys.* **49** (1984) 1933–1942.
18. X. Zhu and G. McMechan, *Geophys.* **56** (1991) 328–339.